

See discussions, stats, and author profiles for this publication at: <https://www.researchgate.net/publication/319970162>

One-step synthesis of Ag₂O@Mg(OH)₂ nanocomposite as an efficient scavenger for iodine and uranium

Article in *Journal of Colloid and Interface Science* · September 2017

DOI: 10.1016/j.jcis.2017.09.073

CITATIONS

0

READS

54

5 authors, including:



Yuanyuan Chen

University of Science and Technology of China

2 PUBLICATIONS **0** CITATIONS

[SEE PROFILE](#)



Sheng-Hui Yu

Shaanxi University of Science and Technology

9 PUBLICATIONS **23** CITATIONS

[SEE PROFILE](#)



Gen-Tao Zhou

University of Science and Technology of China

70 PUBLICATIONS **1,132** CITATIONS

[SEE PROFILE](#)

Some of the authors of this publication are also working on these related projects:



heavy metals treatment [View project](#)



Contents lists available at ScienceDirect

Journal of Colloid and Interface Science

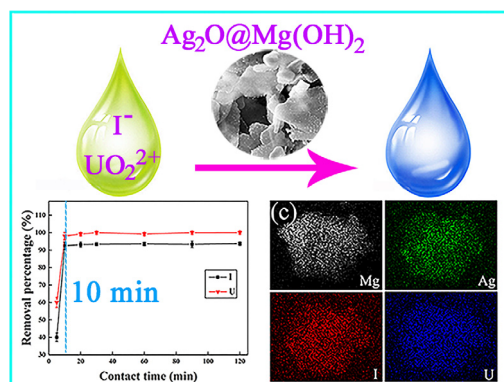
journal homepage: www.elsevier.com/locate/jcis

Regular Article

One-step synthesis of $\text{Ag}_2\text{O}@Mg(\text{OH})_2$ nanocomposite as an efficient scavenger for iodine and uranium

Yuan-Yuan Chen^a, Sheng-Hui Yu^a, Qi-Zhi Yao^{b,*}, Sheng-Quan Fu^c, Gen-Tao Zhou^{a,*}^a CAS Key Laboratory of Crust-Mantle Materials and Environments, School of Earth and Space Sciences, University of Science and Technology of China, Hefei 230026, PR China^b School of Chemistry and Materials Science, University of Science and Technology of China, Hefei 230026, PR China^c Hefei National Laboratory for Physical Sciences at Microscale, University of Science and Technology of China, Hefei 230026, PR China

GRAPHICAL ABSTRACT



ARTICLE INFO

Article history:

Received 9 August 2017

Revised 18 September 2017

Accepted 20 September 2017

Available online 21 September 2017

Keywords:

 $Mg(\text{OH})_2$ nanoplates $\text{Ag}_2\text{O}@Mg(\text{OH})_2$ nanocomposite

One-step method

Simultaneous removal

 I^- and UO_2^{2+}

ABSTRACT

Ag_2O nanoparticles anchored on the $Mg(\text{OH})_2$ nanoplates ($\text{Ag}_2\text{O}@Mg(\text{OH})_2$) were successfully prepared by a facile one-step method, which combined the $Mg(\text{OH})_2$ formation with Ag_2O deposition. The synthesized products were characterized by a wide range of techniques including powder X-ray diffraction (XRD), field emission scanning electron microscopy (FESEM), transmission electron microscopy (TEM), selected area electron diffraction (SAED), and nitrogen physisorption analysis. It was found that Ag_2O nanoparticles anchored on the $Mg(\text{OH})_2$ nanoplates show good dispersion and less aggregation relative to the single Ag_2O nanoaggregates. In addition, iodide (I^-) removal by the $\text{Ag}_2\text{O}@Mg(\text{OH})_2$ nanocomposite was studied systematically. Batch experiments reveal that the nanocomposite exhibits extremely high I^- removal rate (<10 min), and I^- removal capacity is barely affected by the concurrent anions, such as Cl^- , SO_4^{2-} , CO_3^{2-} and NO_3^- . Furthermore, I^- and UO_2^{2+} could be simultaneously removed by the nanocomposite with high efficiency. Due to the simple synthetic procedure, the excellent removal performances for iodine and uranium, and the easy separation from water, the $\text{Ag}_2\text{O}@Mg(\text{OH})_2$ nanocomposite has real potential for application in radioactive wastewater treatment, especially during episodic environmental crisis.

© 2017 Elsevier Inc. All rights reserved.

* Corresponding authors.

E-mail address: gtzhou@ustc.edu.cn (G.-T. Zhou).

1. Introduction

Recently, the concern on nuclear waste leakage has drawn increasing attention globally since the nuclear accident at Fukushima in 2011 [1]. The radioactive iodine is one kind of the major by-products of uranium and plutonium fission, and the half-life of radioiodine isotope differs from about 8 days (^{131}I) to 1.6×10^7 years (^{129}I) [2–4]. In addition, radioactive iodine is also widely applied to the diagnosis and treatment of various diseases [5,6]. For instance, ^{131}I , often used in hyperthyroidism, thyroid cancer diagnosis and metabolic therapies [7], is habitually dumped into domestic sewer system, and thus is one of the radionuclides most often detected in the medical sewage [8–10]. Because of the non-selective uptake of iodine isotope by human body, radioactive iodine can be accumulated in the human thyroid gland and lead to increase of metabolic disorders, mental retardation, and thyroid cancer, especially for children [11]. Studies on iodine speciation in aqueous environment have demonstrated that pH, salinity, natural organic matter (NOM) and microorganisms are involved in regulating iodine biogeochemical processes [11,12]. Dominant iodine species include iodide (I^-), iodate (IO_3^-), and organo iodine in the natural environment [13,14]. It has been proposed that I^- is the major species in deep radioactive waste repositories and is stable almost over the entire pH range [4,15]. Due to the poor removal abilities of many nanomaterials to anions, the implementation in developing nanomaterials for the efficient immobilization of radioactive iodine anions, especially I^- , from aqueous environment is lagged [15].

Various nanomaterials, such as organic anion exchange resins [16], clay minerals [15,17], Ag-based materials [18–27], layered double hydroxide [28–31], and compounds containing Hg^{2+} [32], Bi^{3+} [4,33], and Cu^+ [34,35], have been recently studied for the treatment of water contaminated by radioactive I^- . However, organic anion resin are unstable under high dose of radiation and elevated temperatures [36], and many inorganic materials often display relatively low removal capacities and slow uptake kinetics [4,24]. Among these materials, Ag_2O is a potential capture agent for radioactive I^- because of the efficient I^- immobilization by Ag_2O to form AgI precipitate. Nevertheless, it has been found that the smaller the nanoparticles are, the higher the tendency of aggregation becomes, which stems from high surface free energy. The formation of aggregates could significantly decrease the surface area of Ag_2O , thereby leading to a sharp deterioration of activity and efficiency [24]. Therefore, using Ag_2O directly for the treatment of radioactive I^- is impractical. Anchoring Ag_2O nanoparticles onto the supported-materials could reduce the aggregation of Ag_2O nanoparticles, and thus may improve their performance in I^- uptake. Recently, many Ag_2O -based nanocomposites have been reported for the efficient removal of radioactive I^- [19–24]. For example, Ag_2O anchored titanate nanotubes, nanofibers and nanolamina have been reported to act as scavengers for highly efficient and selective capture of I^- [19,20]. In addition, Ag_2O grafted sodium niobate nanofibers also showed good removal performance for I^- [24]. These findings have provided new insights into the efficient capture of radioactive iodine. However, some shortcomings of the reported supported-materials, such as complexity of preparation, high cost and sensitivity to solution pH, still limit the wide application of Ag_2O . Thus, the search for new substrate that is facilely synthesized and stable under complicated conditions is still crucial and urgent.

As a nontoxic, low cost and environmentally friendly material, nanoscale brucite (nano- $\text{Mg}(\text{OH})_2$) is widely applied in the environmental remediation [37–43]. For instance, Li et al. reported that self-supported flowerlike $\text{Mg}(\text{OH})_2$ could recycle rare earth elements from low concentration wastewater via ion-exchange [37].

A strategy was proposed by Liu et al. to simultaneously realize both the recycle of $\text{Mg}(\text{OH})_2$ nanoadsorbent and enrichment of diluted $\text{Cr}(\text{VI})$ from wastewater, which was based on the reversible phase transformation between platelet-like $\text{Mg}(\text{OH})_2$ nanoparticles and rod-like $\text{MgCO}_3 \cdot 3\text{H}_2\text{O}$ bulk crystals [39]. In addition, $\text{Mg}(\text{OH})_2$ micro/nanorods also showed highly selective adsorption capacity and fast adsorption rate for the removal of dilute anionic dye, and the adsorbed dye was successfully desorbed by carbonation, resulting in a ~ 4000 fold enrichment of the dye solution [40]. It's well established that nano- $\text{Mg}(\text{OH})_2$, having a hexagonal symmetry structure [44], usually exhibits nanoplate-like morphology with a large specific surface area [45], which can potentially provide an ideal substrate for Ag_2O nanoparticle loading. Moreover, nano- $\text{Mg}(\text{OH})_2$ could be facilely synthesized by the hydrolysis of periclase (MgO), which is abundant in nature, and thus could be helpful to greatly reduce the preparation cost. In particular, Chen et al. recently reported that a high uranium removal capacity of $\text{Mg}(\text{OH})_2$ could be found when the initial uranium concentration crosses over a threshold [46]. Therefore, $\text{Mg}(\text{OH})_2$ nanoplates can not only act as a substrate for Ag_2O nanoparticles, but also remove uranium efficiently from solution. That is, Ag_2O coupled with $\text{Mg}(\text{OH})_2$ can be potentially applied to the simultaneous removal of iodine and uranium from radioactive wastewater. However, to the best of our knowledge, no research has been reported on the removal of radioactive iodine, especially on the simultaneous removal of iodine and uranium, by $\text{Ag}_2\text{O}@\text{Mg}(\text{OH})_2$ nanocomposite.

Herein, $\text{Ag}_2\text{O}@\text{Mg}(\text{OH})_2$ nanocomposite is successfully prepared by a facile one-step method, which combined the $\text{Mg}(\text{OH})_2$ formation with Ag_2O deposition, and the removal ability of the nanocomposite to I^- is systematically investigated. In addition, considering the fact that multiple radionuclides can coexist in radioactive wastewater, the simultaneous removal of I^- and UO_2^{2+} by the nanocomposite is also investigated.

2. Materials and methods

2.1. Materials

All chemicals are commercially available and used as received without further purification. AgNO_3 , MgO and NaI were purchased from Sinopharm Chemical Reagent Co., Ltd., and are of analytical grade. $\text{UO}_2(\text{NO}_3)_2 \cdot 6\text{H}_2\text{O}$ was obtained from Beijing Chemical Industry. Analytical grade nitric acid (HNO_3) and sodium hydroxide (NaOH) were used to adjust the pH whenever necessary. Deionized water was used in all experiments.

2.2. Preparation of $\text{Ag}_2\text{O}@\text{Mg}(\text{OH})_2$ nanocomposite

The $\text{Ag}_2\text{O}@\text{Mg}(\text{OH})_2$ nanocomposite was synthesized using a facile one-step method at room temperature. In a typical procedure, 0.46 g (2.71 mmol) AgNO_3 was first dissolved into 50 mL of deionized water. Then 0.40 g of MgO (10 mmol) was slowly added into the AgNO_3 solution under continuously stirring. After 12 h of stirring, the precipitate was collected by centrifugation, washed three times with deionized water, and then dried in the vacuum at 60 °C for 12 h. The finally obtained precipitate was designated as sample SOMH-1. For comparison, different amounts of AgNO_3 (0.095 and 0.85 g) were used to obtain $\text{Ag}_2\text{O}@\text{Mg}(\text{OH})_2$ nanocomposite with different Ag_2O loadings by the same procedures, which were labeled as samples SOMH-2 and SOMH-3, respectively. The loading of Ag_2O in the nanocomposite is determined by inductively coupled plasma atomic emission spectroscopy (ICP-AES, optima 7300 DV) after sample dissolved by HNO_3 solution. In addition, $\text{Mg}(\text{OH})_2$ nanoplates were prepared under the same experimental

conditions but without addition of AgNO_3 . Unsupported Ag_2O nanoparticles were synthesized by adding NaOH dropwise into the AgNO_3 solution until the pH value reached 9.8 and stirring for 12 h at room temperature. The detailed contents of reactants and loaded Ag_2O are listed in Table S1.

2.3. Characterizations

Several analytical techniques were used to characterize the synthesized products. The structure and phase composition of the synthesized products were analyzed by X-ray powder diffraction (XRD) with a Japan MXPAHF X-ray diffractometer equipped with graphite-monochromatized $\text{Cu K}\alpha$ irradiation ($\lambda = 1.541841 \text{ \AA}$), with a scanning rate of $0.01^\circ \text{ s}^{-1}$ in the 2θ range of $10\text{--}70^\circ$. The size and morphology of the products were observed by JEOL JSM-6700F cold field-emission scanning electron microscopy (FESEM) and GeminiSEM 500 schottky field-emission scanning electron microscopy. The elements distribution of the products were analyzed by X-MAX^N energy-dispersive X-ray spectroscopy (EDX). Transmission electron microscopy (TEM) images were obtained on a Hitachi model H-800 transmission electron microscope with an accelerating voltage of 200 kV. Nitrogen sorption data was performed at a Micromeritics Tristar II 3020M automated gas adsorption analyzer utilizing Barrett-Emmett-Teller (BET) calculation for surface area. The zeta potential of the materials was determined with Nano-Brook Omni Zeta Potential Analyzer (Brookhaven Instruments Corporation, America).

2.4. I^- removal experiments

Considering the toxicity of radioactive iodine isotope, the removal experiments were carried out with non-radioactive ^{127}I as surrogate. A stock solution containing I^- was prepared by dissolving NaI in deionized water, and a series of solutions used during the experiments were prepared by diluting the stock to the desired concentrations. All batch experiments were carried out by mixing 0.05 g of the nanocomposite material with 50 mL of I^- solution under stirring at room temperature. The solution pH was adjusted using diluted HNO_3 and NaOH solution. The effects of pH, contact time, equilibrium concentration of I^- , and coexistent anions (Cl^- , SO_4^{2-} , CO_3^{2-} and NO_3^-) on I^- removal performance were systematically investigated by the same procedures. The precipitate after I^- immobilization was separated from the solution by centrifugation at 10,000 rpm for 10 min. The residual concentration of I^- in the supernatant was determined using a UV-Vis spectrophotometer (TU-1901, Beijing Purkinje General Instrument Co., Ltd., China) at 226 nm. The coefficient of determination value R^2 calculated from the calibration line is 0.9995. Inductively coupled plasma mass spectrometry (ICP-MS, Plasma Quad3) was used when the residual I^- concentration is of trace. All removal experiments were run in triplicate, and averaged values were reported. The amount of I^- removed at time t , q_t (mg/g), the amount of I^- removed at equilibrium, q_e (mg/g), and removal percentage $W\%$, were calculated according to following equations, respectively:

$$q_t = \frac{(C_i - C_t)V}{m} \quad (1)$$

$$q_e = \frac{(C_i - C_e)V}{m} \quad (2)$$

$$W\% = \frac{(C_i - C_t)100\%}{C_i} \quad (3)$$

where C_i (mg/L), C_t (mg/L), and C_e (mg/L) are the liquid phase concentration of I^- at initial, any time t and equilibrium, respectively. V

is the volume of the solution (mL), and m is the mass of the scavenger added (mg).

2.5. Leaching test of I^- -loaded nanocomposite

When the removal of I^- by $\text{Ag}_2\text{O}@ \text{Mg}(\text{OH})_2$ nanocomposite reached the uptake saturation, the samples were collected via centrifuge (10,000 rpm, 10 min) and rinsed with deionized water three times. Then, the obtained precipitate was redispersed into 50 mL of solution with pH value ranging from 3.0 to 7.0, and the suspension was shaken for 72 h at room temperature. Leaching amounts of I^- were determined by ICP-MS measurement.

2.6. Simultaneous removal of I^- and UO_2^{2+}

To study the simultaneous removal performance of $\text{Ag}_2\text{O}@ \text{Mg}(\text{OH})_2$ nanocomposite for iodine and uranium, the test is performed by adding 0.05 g of the nanocomposite into 50 mL of solution containing I^- and UO_2^{2+} . In the kinetic study, iodine and uranium kept fixed concentrations of 200 mg/L respectively, and samples were collected at preset time intervals for measurement. Additionally, the effect of initial uranium concentration on the removal performance for I^- and UO_2^{2+} was also investigated by the same procedures. The residual concentration of iodine and uranium in the solution was determined using UV-vis spectrophotometer and ICP-AES, respectively.

3. Results and discussion

3.1. Characterization of $\text{Ag}_2\text{O}@ \text{Mg}(\text{OH})_2$ nanocomposite

Phase composition and structure of the samples prepared with and without AgNO_3 were firstly identified by XRD technique. Fig. 1a shows the XRD pattern of the sample obtained in the absence of AgNO_3 . All of the diffraction peaks can be well indexed to the hexagonal brucite ($\text{Mg}(\text{OH})_2$) with the lattice parameters $a = 3.130 \text{ \AA}$, $c = 4.710 \text{ \AA}$, and space group $P3m1$ (JCPDS file 86-0441), and no characteristic peaks belonging to periclase (MgO) starting material can be detected, indicating that the MgO powders dispersed in aqueous solution has completely transformed into brucite under current experimental conditions. Fig. 1b depicts the typical XRD pattern of the sample obtained with AgNO_3

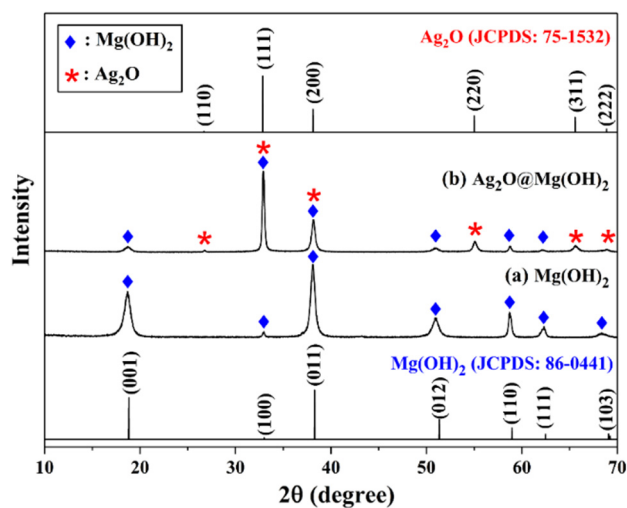


Fig. 1. Representative XRD patterns of the as-synthesized $\text{Mg}(\text{OH})_2$ nanoplates (a) and $\text{Ag}_2\text{O}@ \text{Mg}(\text{OH})_2$ nanocomposite (b). Standard XRD patterns for $\text{Mg}(\text{OH})_2$ (JCPDS: 86-0441) and Ag_2O (JCPDS:75-1532).

(sample SOMH-1 in Table S1). The result reveals the appearance of strong characteristic diffraction peaks belonging to cubic Ag_2O (JCPDS file 75-1532, space group $Pn\bar{3}m$), besides the characteristic diffractions peaks of $\text{Mg}(\text{OH})_2$, indicating the coexistence of Ag_2O and $\text{Mg}(\text{OH})_2$ in the prepared product.

The morphology and surface texture of commercial MgO , and $\text{Mg}(\text{OH})_2$ samples with and without Ag_2O modification were observed by FESEM and TEM. The FESEM observations show that the commercial MgO is mainly aggregates consisting of nanospheres (Fig. S1 and its inset), while the $\text{Mg}(\text{OH})_2$ without Ag_2O modification exhibits a hierarchical architecture assembled by interwoven $\text{Mg}(\text{OH})_2$ nanoplates with a thickness of ca. 5 nm (Fig. 2a and inset B). TEM analyses further reveal that the subunits constructing the hierarchical architectures are quasi hexagonal plates (Fig. 2b), in accordance to the growth habit of brucite crystal. Corresponding SAED patterns of the nanoplates clearly exhibit a set

of similarly regular diffraction spots, and the spots can be indexed as hexagonal brucite with the zone axis $[001]$ (e.g., inset in Fig. 2b), indicating the single-crystal nature of the nanoplates. After MgO powders were dispersed into AgNO_3 solution and stirred for 12 h at room temperature, however, the final precipitate turns into dark brown (Fig. 2c inset A), entirely different from the white $\text{Mg}(\text{OH})_2$ (Fig. 2a inset A). Corresponding SEM results reveal that the product is still a interwoven nanoplate-like morphology (Fig. 2c), but massive nanoparticles can be distinguished from the surface of $\text{Mg}(\text{OH})_2$ nanoplates (Fig. 2c inset B). Combining with its XRD result (Fig. 1b), it can be identified that the nanoparticles should be Ag_2O . Furthermore, the EDX analysis demonstrates that the product contains a large number of O, Mg and Ag, as well as a small amount of Cu and Au (Fig. 2d), here the element Cu comes from copper substrate and Au from the sample preparation of SEM analysis. Meanwhile, the elemental mappings show the

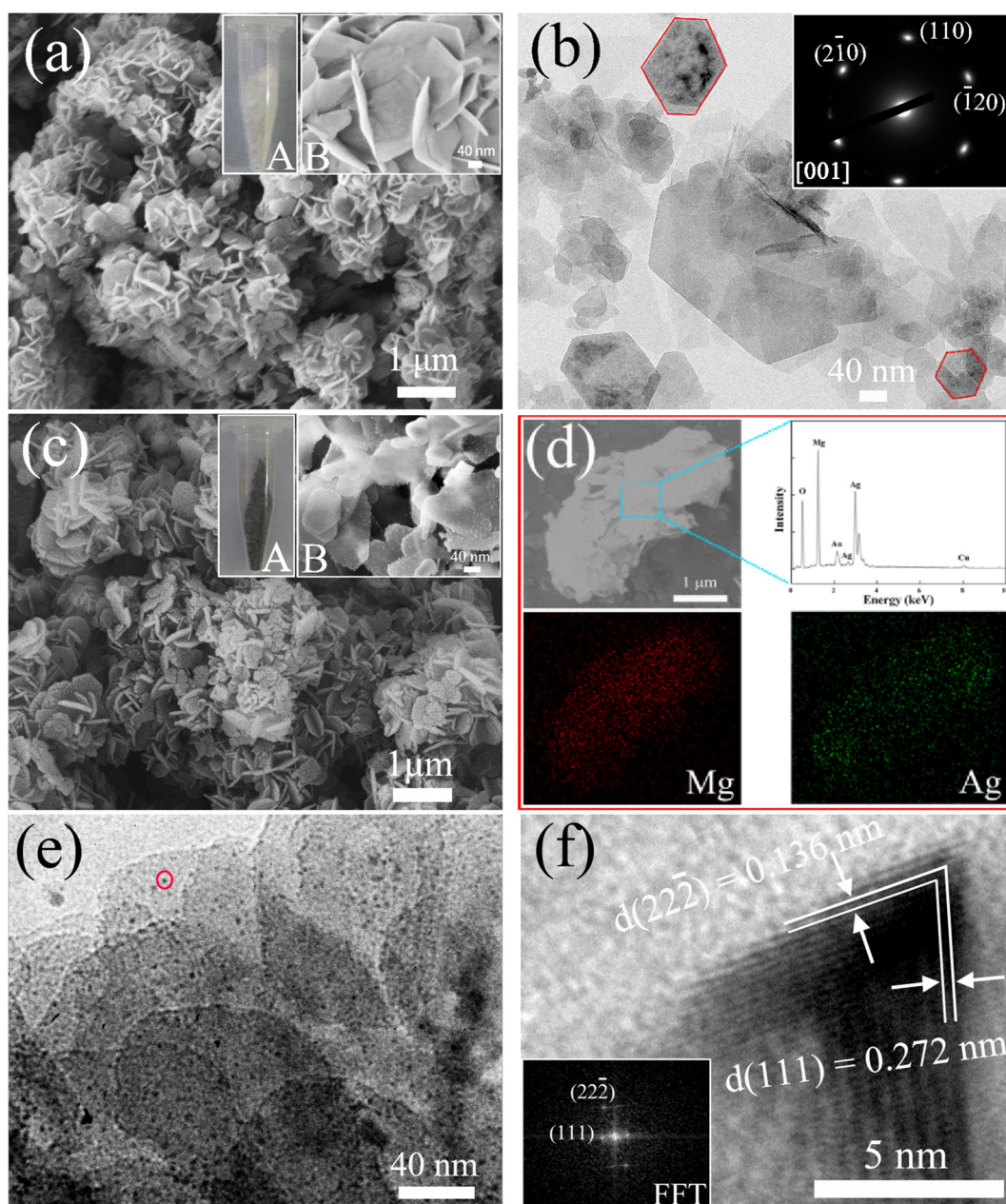


Fig. 2. SEM and TEM images of the $\text{Mg}(\text{OH})_2$ nanoplates (a and b) and $\text{Ag}_2\text{O}@\text{Mg}(\text{OH})_2$ nanocomposite (c and e). The EDX and element mapping analyses of the $\text{Ag}_2\text{O}@\text{Mg}(\text{OH})_2$ nanocomposite (d). A representative HRTEM image of a Ag_2O nanoparticle on the $\text{Mg}(\text{OH})_2$ nanoplate (f).

homogeneous distribution of Mg and Ag in the product, and the density of Mg is far higher than that of Ag (Fig. 2d), indicating that the Ag_2O nanoparticles are uniformly dispersed on the surface of $\text{Mg}(\text{OH})_2$. These results confirm the formation of $\text{Ag}_2\text{O}@Mg(\text{OH})_2$ nanocomposite. Moreover, the microstructures of the $\text{Ag}_2\text{O}@Mg(\text{OH})_2$ nanocomposite are further characterized by TEM and HRTEM, as depicted in Fig. 2e and f. One can find from Fig. 2e that large numbers of nanoparticles are uniformly anchored onto the surfaces of $\text{Mg}(\text{OH})_2$ nanoplates even after a few minutes of ultrasonic treatment, and no separated individuals or aggregates of nanoparticles can be found, indicating the strong affinity between Ag_2O nanoparticles and $\text{Mg}(\text{OH})_2$ nanoplates. Fig. 2e also shows that the average size of the nanoparticles is ca. 5 nm, which can ensure the high exposure of Ag_2O nanocrystals to the contaminated water, and thus a high capture efficiency to I^- ions. The representative HRTEM image of a Ag_2O nanoparticle on the surface of the $\text{Mg}(\text{OH})_2$ nanoplate (circled in Fig. 2e) reveals its single-crystalline nature, owing to their clearly resolved lattice fringes and corresponding fast Fourier transform (FFT) dots (Fig. 2f and its inset). The resolved fringes with interplanar spacing of 0.136 nm and 0.272 nm correspond to (222) and (1 1 1) planes of Ag_2O cubic phase, respectively (Fig. 2f). It can be safely concluded from the aforementioned results that the $\text{Ag}_2\text{O}@Mg(\text{OH})_2$ nanocomposite can be easily harvested by a simple one-step route, and the Ag_2O nanocrystals are homogeneously anchored on the $\text{Mg}(\text{OH})_2$ nanoplates.

The surface structure and composition of the obtained $\text{Mg}(\text{OH})_2$ nanoplates with and without Ag_2O modification was further determined by XPS over the energy range of 0–1350 eV. As shown in Fig. 3a, compared with survey spectrum of $\text{Mg}(\text{OH})_2$, it can be unambiguously seen that pronounced core level peaks of Ag, besides O and Mg, appeared in the survey spectrum of $\text{Ag}_2\text{O}@Mg(\text{OH})_2$ nanocomposite, which is in good accordance with the corresponding results of EDX analysis (Fig. 2d). According to the high resolution scan of Ag 3d (Fig. 3b), the photoelectron peaks at 368.0 and 374.0 eV can be reasonably assigned to the Ag^+ of Ag_2O [23]. The asymmetric O 1s peak can be deconvoluted into three peaks by using XPS peak-fitting program (Fig. 3c). The peaks at 531.17, 532.02 and 532.61 eV could be ascribed to OH^- of $\text{Mg}(\text{OH})_2$ [47,48], the lattice oxygen atoms of the Ag_2O [49,50], and the adsorbed H_2O [51], respectively. This further confirms the successful synthesis of $\text{Ag}_2\text{O}@Mg(\text{OH})_2$ nanocomposite.

The specific surface area of substrate material is a crucial parameter for active removal agent loading, and thus affect the removal capacity and efficiency of the nanocomposite material. Herein, the nitrogen adsorption/desorption analyses of the $\text{Mg}(\text{OH})_2$ nanoplates with and without Ag_2O modification were also investigated. Fig. 4 shows representative N_2 adsorption/desorption isotherms of the samples. From which one can see that both the $\text{Mg}(\text{OH})_2$ nanoplates and $\text{Ag}_2\text{O}@Mg(\text{OH})_2$ nanocomposite show typical IV isotherms with H3 hysteresis loops. As H3 and H4 hystereses are usually found on solids consisting of aggregates or agglomerates of

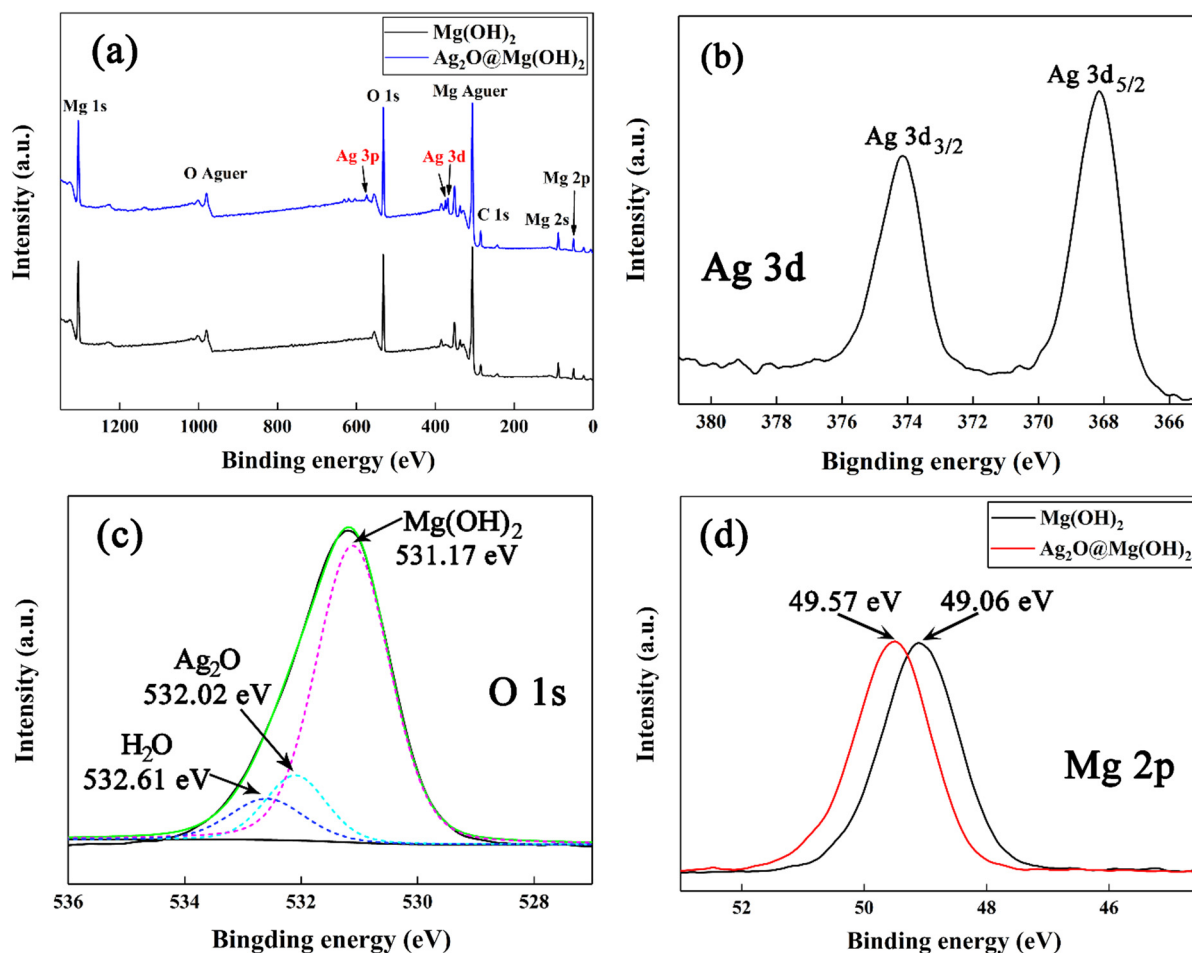


Fig. 3. XPS survey spectra of the as-synthesized $\text{Mg}(\text{OH})_2$ nanoplates and $\text{Ag}_2\text{O}@Mg(\text{OH})_2$ nanocomposite (a). High resolution scans of Ag 3d (b) and O1s (c) spectra of the $\text{Ag}_2\text{O}@Mg(\text{OH})_2$ nanocomposite. High resolution scans of Mg 2p of the $\text{Mg}(\text{OH})_2$ nanoplates with and without modification (d).

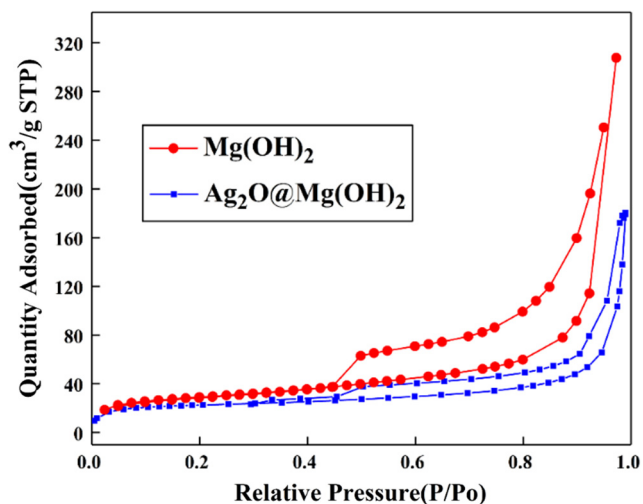


Fig. 4. N_2 adsorption/desorption isotherms of the $Mg(OH)_2$ nanoplates and $Ag_2O@Mg(OH)_2$ nanocomposite.

particles forming slit shaped pores (plates or edged particles like cubes) with uniform (type H4) or nonuniform (type H3) size and/or shape [52], the result further confirms that both the prepared $Mg(OH)_2$ nanoplates and $Ag_2O@Mg(OH)_2$ nanocomposite are hierarchically structured. The BET specific surface areas calculated from N_2 adsorption/desorption isotherms are $105.60 \text{ m}^2/\text{g}$ for the $Mg(OH)_2$ nanoplates and $78.19 \text{ m}^2/\text{g}$ for the $Ag_2O@Mg(OH)_2$ nanocomposite, respectively. The large specific surface area and nanoplate-like morphology of the $Mg(OH)_2$ indicates that the $Mg(OH)_2$ nanoplates have abundant space and site available for the dispersion of Ag_2O nanoparticles without aggregation, and thus could significantly improve I^- removal efficiency and capacity. In addition, the surface area decrease of $Ag_2O@Mg(OH)_2$ nanocomposite, compared with that of the $Mg(OH)_2$, could be ascribed to the formation of Ag_2O nanoparticles on the surface of $Mg(OH)_2$ nanoplates.

In order to understand the formation details of $Ag_2O@Mg(OH)_2$ nanocomposite, the pH evolution of reaction system for $Mg(OH)_2$ nanoplates or $Ag_2O@Mg(OH)_2$ nanocomposite (sample SOMH-1) was first monitored over time. As shown in Fig. S2, for the system of $Mg(OH)_2$ nanoplates, the pH quickly increases from 6.7 to 10.8 within 5 min, and then keeps a constant value. This is because MgO are easily hydrolyzed to generate $Mg(OH)_2$ [53], and the

formed $Mg(OH)_2$ will partially dissociate to produce Mg^{2+} and OH^- ions, leading to a quick rise in solution pH. For $Ag_2O@Mg(OH)_2$ nanocomposite system, a similar evolution phenomenon can be observed. Nevertheless, note that the pH gradually decreases from 10.4 to 9.8 after 5 min of reaction (Fig. S2), indicative of the initial formation of $Mg(OH)_2$ nanostructured substrates and subsequent deposition of Ag_2O nanoparticles. Because of the dissociation of initially formed $Mg(OH)_2$ nanoplates, the concentration of OH^- ions on the surfaces and around $Mg(OH)_2$ nanoplates may be relatively higher than those in solution. As a consequence, Ag^+ ions in aqueous solution can combine with the dissociated OH^- to form insoluble hydroxides ($AgOH$) depositing on the surface of $Mg(OH)_2$ nanoplates. As we know, $AgOH$ is unstable [20], and thus it would further dehydrate and finally transform into stable Ag_2O . With the continuous consumption of the dissociated OH^- by Ag^+ , the solution pH gradually decreases until the complete deposition of Ag^+ (schematically depicted as Process 1 in Fig. 5). This can also be supported by the positive correlation of the deposited Ag^+ with the dissolved Mg^{2+} in solution (Fig. S3). Nevertheless, Fig. S3 also unambiguously shows that the molar ratio of the dissolved Mg^{2+} to the deposited Ag^+ is much lower than the stoichiometric ratio of 0.5, indicating that other processes may be involved in the deposition of Ag_2O . In this context, the Mg 2p XPS analyses for the $Mg(OH)_2$ nanoplates with and without Ag_2O modification were further performed. The high resolution spectra show that the binding energy of Mg 2p in the nanocomposite shifts to higher energy side relative to $Mg(OH)_2$ nanoplates (Fig. 3d). It can be due to the formation of $Mg-O-Ag$ bonds in the nanocomposite, leading to the decrease of electron cloud density of $Mg-O$ bond. Similar results have been also reported by Xiong et al. [54]. In their work, the binding energy of Mg 1s was observed to shift to higher energy side after adsorption of Pb by MgO , which was ascribed to the formation of $Mg-O-Pb$ bond in the adsorbed product. Zhu's group also reported that the Ag_2O nanocrystals can be firmly anchored onto the external surface of the titanate nanomaterials (nanolamina, nanotubes and nanofibers) by sharing oxygen atoms at well-matched interfaces between the two phases [19,20,22]. It's well established that $Mg(OH)_2$ possess a hexagonal layered basic structure [55,56]. Specifically, one layer of magnesium cations are sandwiched between every two layers of hydroxyl groups, and $OH-Mg-OH$ layers is along the [0 0 1] direction, perpendicular to the nanoplates (e.g., Figs. 2b and 5) [55,57]. High exposure of active hydroxyl groups have high affinity to Ag^+ ions, thereby forming Ag_2O by sharing O with Mg atoms, and finally offering another possible route for the deposition of Ag_2O onto

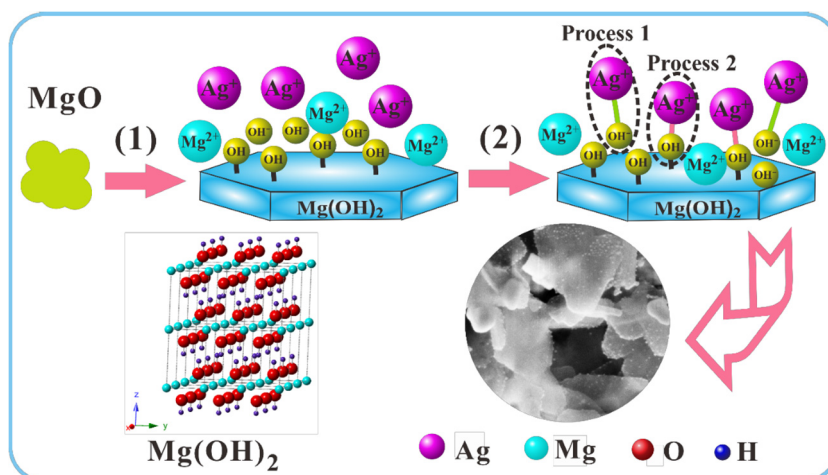
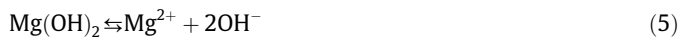


Fig. 5. Schematic illustration for synthesis of the $Ag_2O@Mg(OH)_2$ nanocomposite.

the $\text{Mg}(\text{OH})_2$ nanoplates (schematically depicted as Process 2 in Fig. 5). Therefore, a plausible formation mechanism of the $\text{Ag}_2\text{O}@\text{Mg}(\text{OH})_2$ nanocomposite is proposed, and schematically illustrated in Fig. 5. The corresponding chemical reactions involved in the formation of the nanocomposite are formulated as follows:



3.2. Removal of I^- by $\text{Ag}_2\text{O}@\text{Mg}(\text{OH})_2$ nanocomposite

The pH value of the solution is one of the factors most affecting I^- removal behavior by inducing the changes in the surface charges of the scavengers [4,58]. Thus, the pH-dependent experiments were first carried out at initial pHs from 3.0 to 12.0, initial I^- concentration 200 mg/L, and contact time 6 h. The removal percentages of the $\text{Ag}_2\text{O}@\text{Mg}(\text{OH})_2$ nanocomposite (sample SOMH-1) to I^- approach to 100% and are nearly unchanged over the tested pH range (Fig. 6a). Such an excellent removal performance could be attributed to the coupled existence of Ag_2O nanoparticles and $\text{Mg}(\text{OH})_2$ nanosubstrates. Usually, Ag_2O nanoparticles can partly

dissolve at acidic medium ($\text{pH} < 6.0$), and thus their abilities to capture I^- anions decrease [24]. While, the $\text{Mg}(\text{OH})_2$ substrate with basic nature has a level-off effect on the pH of the I^- removal system, avoiding the dissolution of Ag_2O nanoparticulates. Here, the final pHs of solution after removal treatment are measured to be ca. 9.0 at initial pH 3.0–7.0 (Fig. 6a), confirming the level-off effect of $\text{Mg}(\text{OH})_2$ on the solution pH. It appears that the present $\text{Ag}_2\text{O}@\text{Mg}(\text{OH})_2$ nanocomposite exhibits very high removal ability to I^- anions over a wide pH range, which can circumvent the drawbacks of previously reported Ag_2O -based scavengers that were only used within the limited pH range [19,20,24], and thus can be potentially applied to practical radioactive wastewater treatment. Moreover, according to the pH-dependent experiments, a neutral pH 7.0 is selected in the following removal experiments.

The effect of contact time on the removal of I^- was investigated at pH 7.0, initial I^- concentration 200 mg/L, and the contact times ranging from 5 to 150 min. Fig. 6b shows that the removal percentage of the $\text{Ag}_2\text{O}@\text{Mg}(\text{OH})_2$ nanocomposite (sample SOMH-1) to I^- has reached 60% within the first 5 min, and I^- can be completely removed after subsequent 5 min, exhibiting an extremely high removal efficiency. When I^- concentration further increases to 300 mg/L, the complete removal of I^- is still achieved within 20 min (inset in Fig. 6b). Moreover, under the same conditions, the complete removal of 200 mg/L I^- by single Ag_2O material (Fig. S4a and b) needs more than 30 min (Fig. 6b). The relative lower removal rate of the single Ag_2O can be attributed to the

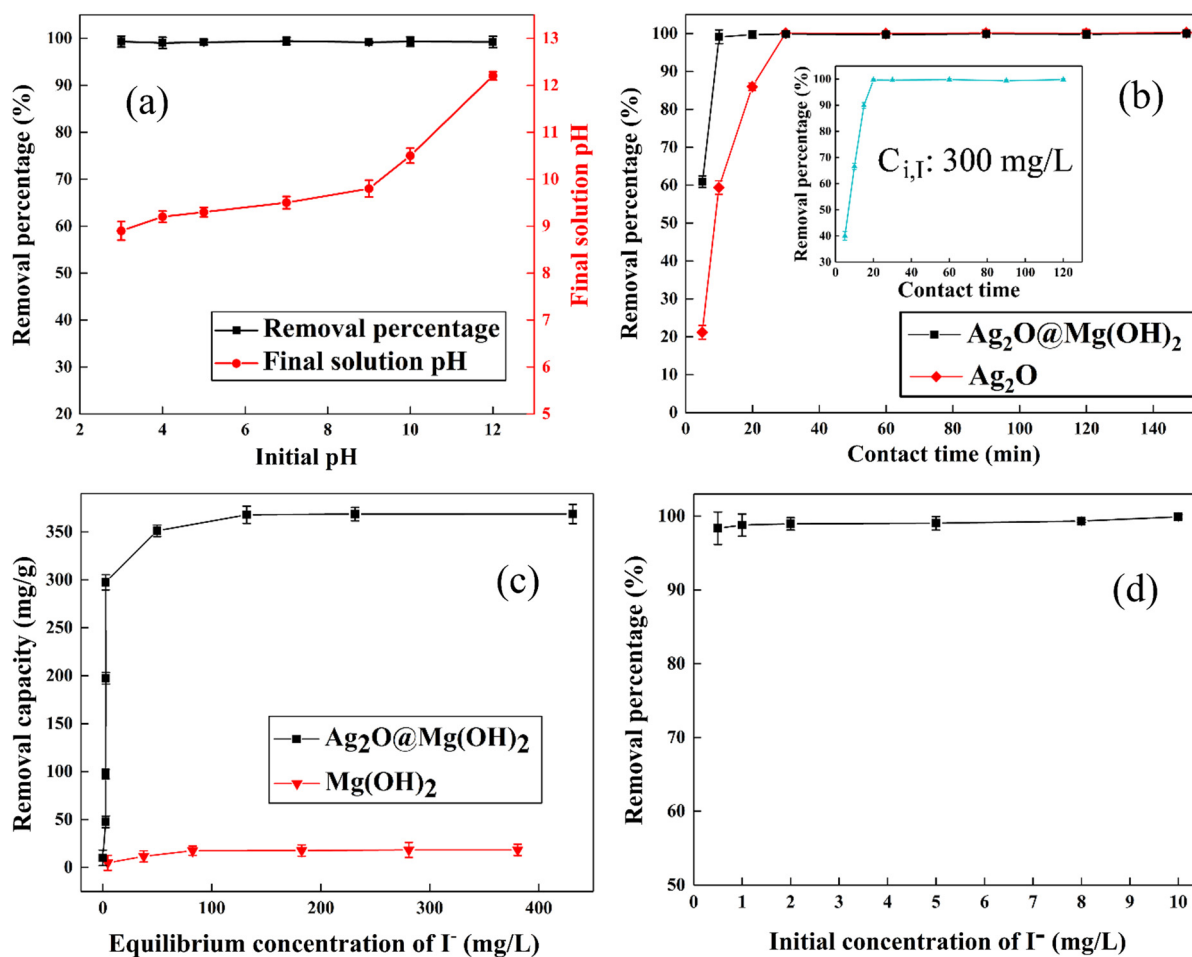


Fig. 6. Effects of pH (a), contact time (b), and low I^- concentration (d) on the removal of I^- by the $\text{Ag}_2\text{O}@\text{Mg}(\text{OH})_2$ nanocomposite. Final solution pH after I^- removal in the pH-dependent experiments (a). I^- sorption isotherms of the $\text{Mg}(\text{OH})_2$ nanoplates and $\text{Ag}_2\text{O}@\text{Mg}(\text{OH})_2$ nanocomposite (c). Inset in Fig. 6b: effect of contact time on the removal of I^- by the $\text{Ag}_2\text{O}@\text{Mg}(\text{OH})_2$ nanocomposite at 300 mg/L of initial I^- concentration.

strong aggregation between the Ag₂O nanoparticles (Fig. S4a and its inset), leading to the decrease in specific surface area and low exposure to I⁻-bearing solution. However, the hierarchical Mg(OH)₂ structure assembled by interleaving nanoplates with large specific surface area, could possess abundant space for the deposition of Ag₂O nanoparticles, avoiding the aggregation of Ag₂O nanoparticles (Fig. 2e) and thus ensuring a high exposure of Ag₂O nanoparticles to I⁻ anions. As a result, a high I⁻ removal efficiency can be harvested. In addition, it is well known that the surface charge of material is neutral at the point of zero charge (PZC), and the surface is positively charged below the pH_{pzc}. Here, the pH_{pzc} of Mg(OH)₂ nanoplates and Ag₂O@Mg(OH)₂ nanocomposite were also measured, respectively. The results show that the pHs at the PZC are 11.2 for Mg(OH)₂ nanoplates, which is consistent with the previous research [59,60], and 11.7 for the nanocomposite (Fig. S5). Such a high pH_{pzc} of the nanocomposite facilitates the fast removal of I⁻ anions due to the strong electrostatic attraction between I⁻ and the nanocomposite.

Moreover, the I⁻ equilibrium sorption isotherms of the nanocomposite and Mg(OH)₂ nanoplates were determined at pH 7.0 and contact time 6 h, respectively. As shown in Fig. 6c, the maximum removal capacity of the nanocomposite to I⁻ is about 368.60 mg/g, and is significantly higher than that of the Mg(OH)₂ nanoplates (19.52 mg/g), indicating that the Mg(OH)₂ nanoplates in the nanocomposite mainly act as a substrate for the uniform loading of Ag₂O nanoparticles. The removal capacity of the nanocomposite to I⁻ is also higher than or comparable to those of previously reported Ag₂O-based nanomaterials, such as Ag₂O-layered sodium vanadate (215.96 mg/g) [21], Ag₂O-sodium niobate nanofibers (295.92 mg/g) [24], Ag₂O-Ag/TiO₂ microspheres (213.45 mg/g) [23], and Ag₂O-titanate nanomaterials [nanolamina (431.83 mg/g) [20], nanofibers (571.52 mg/g) and nanotubes (381.13 mg/g) [19]]. In addition, the removal ability to trace I⁻ by the nanocomposite was also investigated. As shown in Fig. 6d, when the initial concentration of I⁻ varies from 1 to 10 mg/L, the removal percentages are nearly 100%, and residual I⁻ concentrations are less than 0.05 mg/L, exhibiting an excellent removal performance of the nanocomposite to trace of I⁻.

The effect of Ag₂O loading in the nanocomposite on the Ag utilization efficiency was further investigated. The actual amount of Ag₂O loaded was obtained from ICP-AES data, and thus the Ag utilization efficiency can be calculated. As listed in Table S2, the average weight percentage of Ag₂O in sample SOMH-1 is measured to be 34.74 wt%, corresponding to a 3.00 mmol Ag atoms per gram for the nanocomposite. Therefore, the theoretical maximum removal capacity of I⁻ goes to be 380.79 mg/g (3.00 mmol/g). According to the actual maximum removal capacity of I⁻ obtained from I⁻ equilibrium sorption isotherms experiment [368.60 mg/g (2.90 mmol/g)], the Ag utilization efficiency of the nanocomposite is up to 96.80%. When the Ag₂O loading decreases from 34.74 wt% (sample SOMH-1) to 11.27 wt% (sample SOMH-2), the Ag utilization efficiency still keeps a very high value of 96.61%. Consequently, Ag₂O loading of the nanocomposite can be adjusted to meet the different needs of variously contaminated water. However, as the Ag₂O loading further increases to 53.41 wt% (sample SOMH-3), the Ag utilization efficiency decreases to 86.26%. The observed behavior can be attributed to the fact that the aggregation of nanoparticles occurs with the further increment of Ag₂O loading, which is verified by the SEM analysis of sample SOMH-3 (e.g., Fig. S6). As a result, the Ag utilization efficiency is limited.

3.3. Mechanism of I⁻ removal by Ag₂O@Mg(OH)₂ nanocomposite

After removal of I⁻ from solution, the final precipitate turns to be bright yellow (inset in Fig. 7a), indicating that AgI precipitation occurs in the nanocomposite. For further unveiling the removal

mechanism of I⁻ by the Ag₂O@Mg(OH)₂ nanocomposite, a series of techniques, including SEM, TEM, EDX and XRD, were used to characterize the sample after I⁻ immobilization. As shown in Fig. 7a, I⁻-loaded nanocomposite still displays a hierarchical structure consisting of interwoven nanoplates, and massive nanoparticles with a mean diameter of ca. 10 nm can be seen on the nanoplates (Fig. 7b). Clearly, the size of nanoparticles after uptake of I⁻ is slightly larger than the initial Ag₂O nanoparticles (Fig. 2e), which is consistent with the previous findings of Yang et al. [19] and Mu et al. [24]. In addition, the corresponding EDX spectrum (Fig. 7c) and element mapping analyses (Fig. 7d) distinctly show the existence of iodine element in the sample, confirming the immobilization of I⁻ by the nanocomposite scavenger. Meanwhile, characteristic diffraction peaks of AgI (JCPDS file 09-0374, space group P6₃mc) can be evidently observed from the XRD pattern of the sample (Fig. 8a), while the diffraction peaks belonging to Ag₂O crystal disappear, further identifying that the I⁻ removal occurs following reaction (8):



Therefore, the almost intact morphology and texture of the nanocomposite after I⁻ immobilization ensure the facile separation of the used scavenger from the solution for ultimate safe disposal, which could make it feasible for practical application.

3.4. Selective uptake and leaching test

In natural waters, some other anions generally coexist with I⁻ [33], and such coexistence may influence the removal behavior of scavengers to I⁻. Cl⁻ is one of the commonest anions found in natural water, especially in the seawater [61]. Furthermore, chlorine and iodine are situated in the same group of periodic table, and thus have similar chemical properties. Herein, the selective uptake experiment of I⁻ by the Ag₂O@Mg(OH)₂ nanocomposite in the presence of Cl⁻ was conducted with various molar ratios of Cl⁻ to I⁻ [I⁻ concentration is fixed to be 50 mg/L (0.39 mmol/L)] and a contact time 6 h. One can find from Fig. 9a that the coexistent Cl⁻ has little effect on the removal capacity of I⁻. Even in the simulated seawater, where the concentration of Cl⁻ is up to 130.40 g/L, 2608 times that of 50 mg/L I⁻ [62], the removal percentage is still over 94% (Fig. 9a). This result should be attributed to the large difference in the Gibbs energy of the reactions between Ag₂O and I⁻, and Ag₂O and Cl⁻. The energy for the reactions between Ag₂O and I⁻ (-32 kJ/mol) is lower than that for the reaction between Ag₂O and Cl⁻ (+41 kJ/mol) [19,20]. Evidently, the reaction with I⁻ is thermodynamically much more preferred than that with Cl⁻. Moreover, the effects of other common anions, such as SO₄²⁻, CO₃²⁻ and NO₃⁻, on the removal of I⁻ by the Ag₂O@Mg(OH)₂ nanocomposite were also investigated, and the results were depicted in Fig. S7. When the molar ratio of anions SO₄²⁻, CO₃²⁻, or NO₃⁻ to I⁻ is up to 100:1, the removal percentages of I⁻ by the nanocomposite still approach 100%, showing negligible effect of those concurrent anions on the I⁻ removal. In short, it can be concluded that the Ag₂O@Mg(OH)₂ nanocomposite possesses high selectivity to I⁻, indicating a profound potential for radioactive iodine removal in practical environmental wastewater.

In addition, sorption irreversibility is desirable for radioactive waste treatment since it can ensure the stability of the immobilized radioactive species and thus avoid the resultant secondary pollution. Herein, leaching behavior of the used scavenger was studied at initial pHs from 3.0 to 7.0, and agitation time 72 h. It was found that the amount of I⁻ anions released from the used scavenger is very low or even below detection limits over the wide pH range (Fig. 9b). Therefore, the formed AgI-Mg(OH)₂ precipitate shows a good stability after I⁻ sequestration even though the used

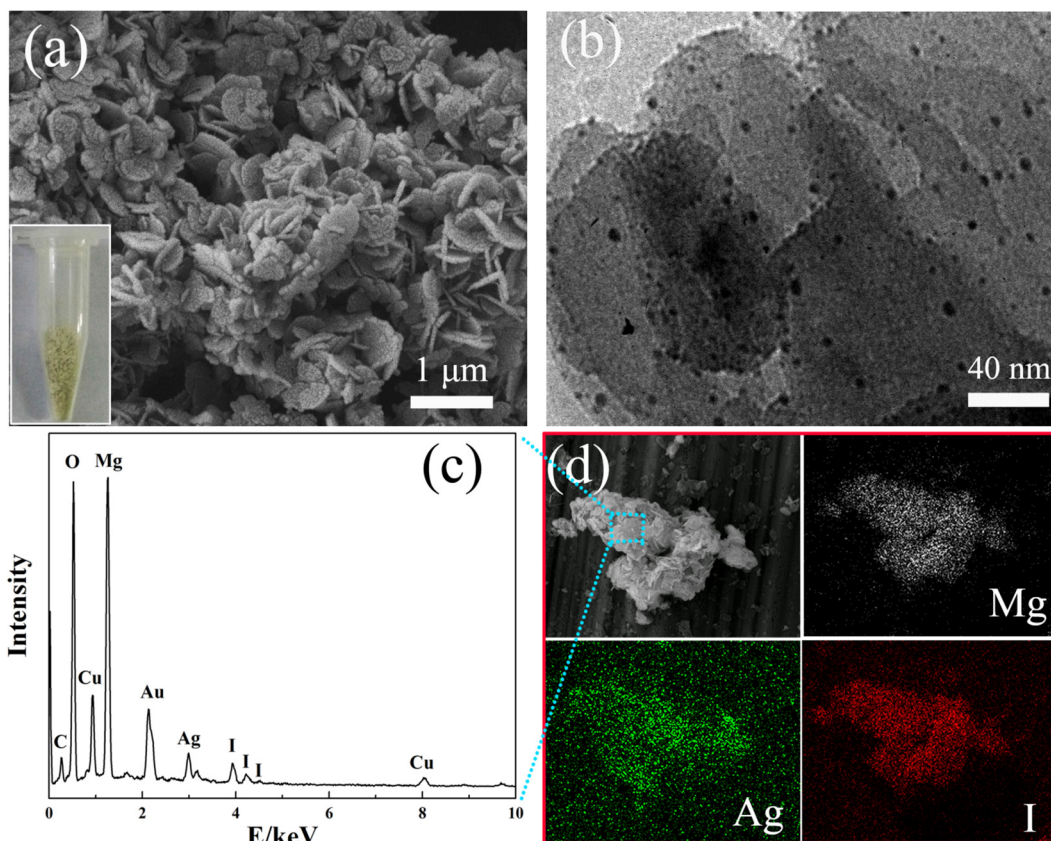


Fig. 7. SEM (a), TEM (b), EDX (c) and element mapping (d) analyses of I^- -loaded nanocomposite.

scavenger encounters the leaching of acidic wastewater after land-fill, and thus reduces the risk of secondary pollution.

3.5. Simultaneous removal of I^- and UO_2^{2+}

In practical contexts, multiple radionuclides, like ^{238}U , ^{137}Cs , ^{131}I , ^{129}I , ^{90}Sr and ^{99}Tc , usually coexist in radioactive wastewater [1,63]. A large number of conventional techniques have been used for the removal of a single class of contaminant individually

[18,23,33,64–66]. However, the different physical and chemical properties of the various contaminant classes make the treatment of radioactive wastewaters more complicated. Thus, the development of facile and green materials to simultaneously remove the multiple radionuclides from wastewaters is urgent.

Herein, the removal tests of iodine and uranium by $Ag_2O@Mg(OH)_2$ nanocomposite were systematically investigated, using I^- and UO_2^{2+} as iodine and uranium sources, respectively. Firstly, the kinetics of the simultaneous removal of I^- and UO_2^{2+} was investigated at contact time 0–120 min, and individual iodine and uranium concentrations 200 mg/L. As shown in Fig. 10a, the removal percentage of UO_2^{2+} is up to 60.73% within first 5 min, exhibiting a higher removal rate than that of I^- (40.41%). After subsequent 5 min, the removal of I^- and UO_2^{2+} synchronously reaches an equilibrium state (96.82% of I^- and 99.39% of UO_2^{2+} removed), indicating that the nanocomposite has still very high removal efficiency to concurrent I^- and UO_2^{2+} ions. Furthermore, the effect of uranium concentration on I^- and UO_2^{2+} removal were examined at contact time 6 h and iodine concentration 200 mg/L. Fig. 10b shows that low concentrations of uranium (<200 mg/L) almost have no effect on the I^- removal. Specifically, as the coexistent uranium concentration is 200 mg/L, the removal percentage of I^- is 96.82%. Even though the coexistent uranium reaches 1000 mg/L, the removal percentage of I^- is still up to 88.67% (Fig. 10b), exhibiting an excellent I^- removal performance in the coexistence of UO_2^{2+} . On the other hand, the removal percentages of UO_2^{2+} always keep very high values, approaching to 100%, over the tested uranium concentration range (Fig. 10b). These results indicate that the $Ag_2O@Mg(OH)_2$ nanocomposite has an outstanding performance for simultaneous removal of I^- and UO_2^{2+} .

In order to ascertain the individual role of Ag_2O and $Mg(OH)_2$ in the nanocomposite played in I^- and UO_2^{2+} simultaneous removal,

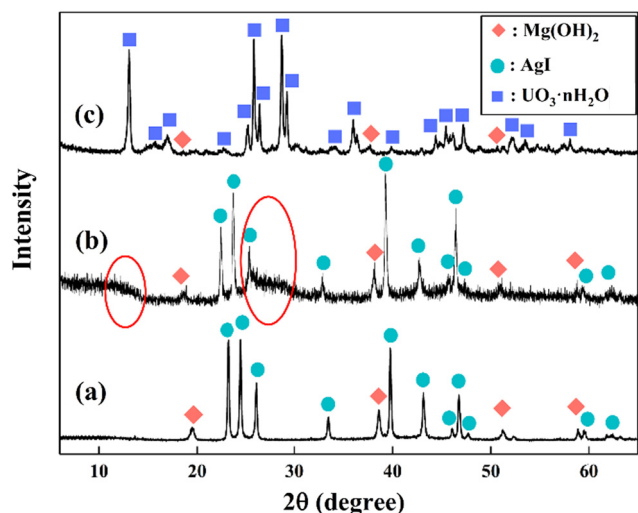


Fig. 8. XRD patterns of I^- -loaded nanocomposite (a), I^- and UO_2^{2+} -loaded nanocomposite (b), and UO_2^{2+} -loaded $Mg(OH)_2$ (c).

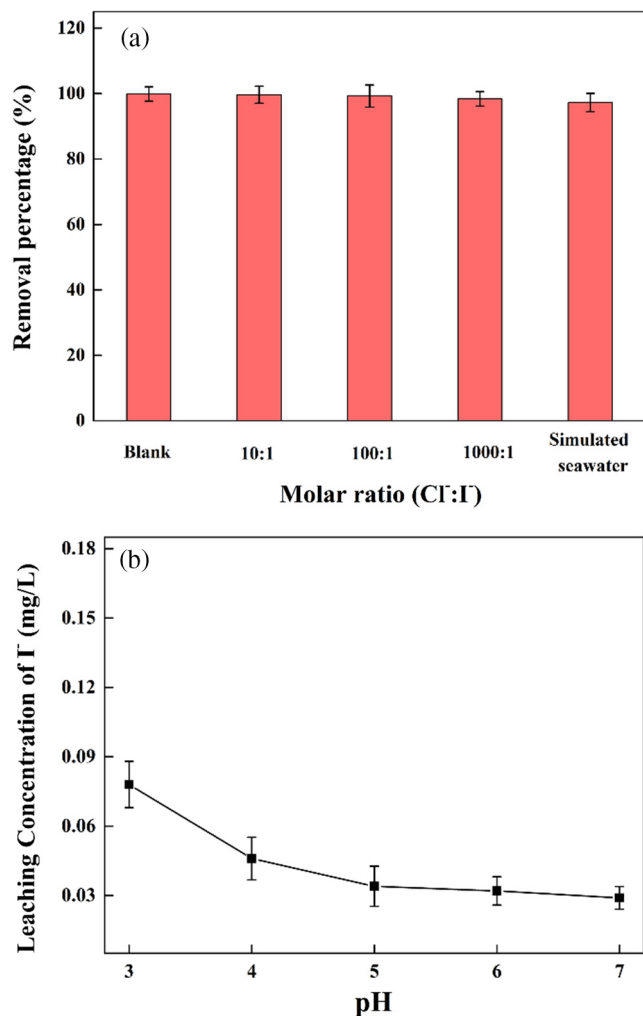


Fig. 9. Effect of Cl⁻ concentration on the removal of I⁻ by the Ag₂O@Mg(OH)₂ nanocomposite (a), and effect of pH on the leaching amount of I⁻ from the used scavenger in water (b).

the removal behaviors of Ag₂O nanoparticles and Mg(OH)₂ nanoplates to UO₂²⁺ were investigated, respectively. It can be distinctly observed from Fig. 10c that Mg(OH)₂ nanoplates show excellent removal performance to UO₂²⁺, while Ag₂O nanoparticles exhibit negligible removal to I⁻. Combined with the excellent I⁻ removal of the Ag₂O@Mg(OH)₂ nanocomposite and negligible I⁻ removal of Mg(OH)₂ nanoplates, it can be concluded that Ag₂O and Mg(OH)₂ in the nanocomposite system play different roles in the simultaneous removal of I⁻ and UO₂²⁺, and Ag₂O nanoparticles and Mg(OH)₂ substrate are responsible for the removal of I⁻ and UO₂²⁺, respectively. Therefore, concurrent I⁻ and UO₂²⁺ ions can be simultaneously removed by the Ag₂O@Mg(OH)₂ nanocomposite from aqueous solution. In addition, for further understanding the simultaneous removal details of I⁻ and UO₂²⁺, a wide range techniques, including SEM, EDX and XRD, were used to characterize the used nanocomposite. Fig. S8a and its inset reveals that the nanocomposite after removal treatment still exhibits interwoven nanoplate-like morphology with massive nanoparticles. Corresponding EDX (inset in Fig. S8b) and element mapping analyses (Fig. S8b and c) clearly show the coexistence of iodine and uranium with homogeneous distribution areas, confirming the simultaneous immobilization of the two elements by the nanocomposite. Furthermore, XRD analysis reveals that except for the characteristic diffraction peaks belonging to Mg(OH)₂ and AgI, two extra weak

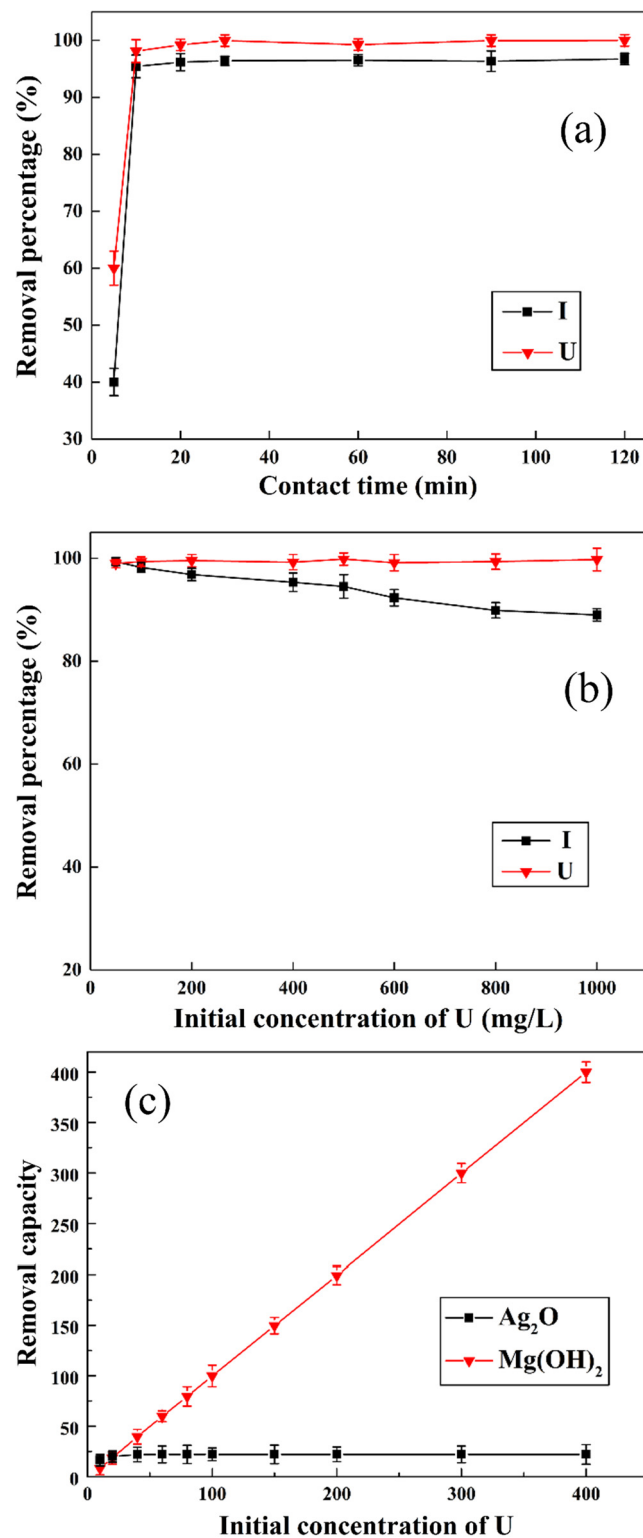


Fig. 10. Effects of contact time (a) and initial uranium concentration (b) on the simultaneous removal of I⁻ and UO₂²⁺ by the Ag₂O@Mg(OH)₂ nanocomposite. (c) Effect of initial uranium concentration on the uranium removal capacity of Ag₂O nanoparticles and Mg(OH)₂ nanoplates, respectively.

and broad peaks near 12° and 26° occur in the used nanocomposite, as highlighted by red circles in Fig. 8b. Similar finding has been reported by Chen et al. [46]. They investigated the sorption interaction between nano-Mg(OH)₂ and uranyl in water, and suggested the two weak and broaden diffraction peaks as a uranium-rich

phase. In order to further confirm the uranium-rich phase, the synthesized $\text{Mg}(\text{OH})_2$ nanoplates (Fig. 2a and b) were added into 4000 mg/L uranium solution and stirred for 24 h for the sufficient sorption. After that, the solution was centrifuged to obtain the precipitate. The corresponding XRD result demonstrates that the main phase is metaschoepite ($\text{UO}_3 \cdot n\text{H}_2\text{O}$) (JCPDF 43-0364) in addition to $\text{Mg}(\text{OH})_2$ (Fig. 8c). Therefore, the uranium-rich phase formed on the surface of $\text{Mg}(\text{OH})_2$ nanoplate should be metaschoepite. Considering the facile preparation process and excellent performance in simultaneous removal of iodine and uranium, the $\text{Ag}_2\text{O}@/\text{Mg}(\text{OH})_2$ nanocomposite can be potentially used in practical radioactive wastewater treatment.

4. Conclusion

In summary, the hierarchical $\text{Ag}_2\text{O}@/\text{Mg}(\text{OH})_2$ nanocomposite was successfully prepared via a facile one-step method, and the surface deposition of Ag_2O nanoparticles occurred by the combination of Ag^+ with OH^- ions and subsequent decomposition from AgOH to Ag_2O on the preformed $\text{Mg}(\text{OH})_2$ nanoplates, as well as the formation of $\text{Mg}-\text{O}-\text{Ag}$ bonds on the surface of $\text{Mg}(\text{OH})_2$ nanoplates, finally leading to $\text{Ag}_2\text{O}@/\text{Mg}(\text{OH})_2$ nanocomposite. The as-synthesized nanocomposite exhibits high removal efficiency, removal capacity, and selectivity uptake to I^- from solution. Ag_2O nanoparticles in the nanocomposite play the main role in the immobilization of I^- by forming AgI precipitate. While the nanoplate-like $\text{Mg}(\text{OH})_2$ not only acts as a valid supported substrate for anchoring and dispersion of Ag_2O nanoparticles, but also has a level-off effect on the pH of the I^- removal system. Therefore, the nanocomposite exhibits very high removal ability to I^- anions over a wide pH range, which can circumvent the drawbacks of previously reported Ag_2O -based scavengers that were only used within the limited pH range [19,20,24]. The formed AgI particles firmly anchor onto the surface of $\text{Mg}(\text{OH})_2$ nanoplates. Thus, the used scavenger can be readily separated from water for safe disposal, and avoid the secondary pollution. Furthermore, the nanocomposite also shows excellent performance for simultaneous removal of iodine and uranium. Therefore, $\text{Ag}_2\text{O}@/\text{Mg}(\text{OH})_2$ nanocomposite is a suitable candidate for the emergent treatment of multiple radionuclides in radioactive wastewater during and after nuclear leakages.

Acknowledgements

This work was partially supported by the Chinese Ministry of Science and Technology (2014CB846003), the Natural Science Foundation of China (41372053, 41572026), and the Fundamental Research Funds for the Central Universities.

Appendix A. Supplementary material

Supplementary data associated with this article can be found, in the online version, at <https://doi.org/10.1016/j.jcis.2017.09.073>.

References

- [1] G. Steinhauser, Fukushima's forgotten radionuclides: a review of the understudied radioactive emissions, *Environ. Sci. Technol.* 48 (2014) 4649–4663.
- [2] P. Slovic, J.H. Flynn, M. Layman, Perceived risk, trust, and the politics of nuclear waste, *Science* 254 (1991) 1603–1607.
- [3] H.A. Robertson, I.R. Falconer, Accumulation of radioactive iodine in thyroid glands subsequent to nuclear weapon tests and the accident at Windscale, *Nature* 184 (1959) 1699–1702.
- [4] L. Liu, W. Liu, X.L. Zhao, D.M. Chen, R.S. Cai, W.Y. Yang, S. Komarneni, D.J. Yang, Selective capture of iodide from solutions by Microrosette-like delta- Bi_2O_3 , *ACS Appl. Mater. Interfaces* 6 (2014) 16082–16090.
- [5] A. Hackshaw, C. Harmer, U. Mallick, M. Haq, J.A. Franklyn, Review: ^{131}I activity for remnant ablation in patients with differentiated thyroid cancer: a systematic review, *J. Clin. Endocrinol. Metab.* 92 (2007) 28–38.
- [6] P.S. Rose, J.P. Smith, R.C. Aller, J.K. Cochran, R.L. Swanson, R.B. Coffin, Medically-derived I-131 as a tool for investigating the fate of wastewater nitrogen in aquatic environments, *Environ. Sci. Technol.* 49 (2015) 10312–10319.
- [7] R. Huang, Z. Zhao, X. Ma, S. Li, R. Gong, A. Kuang, Targeting of tumor radioiodine therapy by expression of the sodium iodide symporter under control of the survivin promoter, *Cancer Gene Ther.* 18 (2011) 144–152.
- [8] P.S. Rose, J.P. Smith, J.K. Cochran, R.C. Aller, R.L. Swanson, Behavior of medically-derived I-131 in the tidal Potomac River, *Sci. Total Environ.* 452 (2013) 87–97.
- [9] F. Jimenez, R. Lopez, R. Pardo, L. Deban, M. Garcia-Talavera, The determination and monitoring of I-131 activity in sewage treatment plants based on A2/O processes, *Radiat. Meas.* 46 (2011) 104–108.
- [10] R. Barquero, M.M. Agulla, A. Ruiz, Liquid discharges from the use of radionuclides in medicine (diagnosis), *J. Environ. Radioact.* 99 (2008) 1535–1538.
- [11] S. Choung, W. Um, M. Kim, M.G. Kim, Uptake mechanism for iodine species to black carbon, *Environ. Sci. Technol.* 47 (2013) 10349–10355.
- [12] S.J. Zhang, C. Xu, D. Creeley, Y.F. Ho, H.P. Li, R. Grandbois, K.A. Schwehr, D.I. Kaplan, C.M. Yeager, D. Wellman, P.H. Santschi, Iodine-129 and Iodine-127 speciation in groundwater at the Hanford Site, US: iodate incorporation into calcite, *Environ. Sci. Technol.* 47 (2013) 9635–9642.
- [13] C. Xu, E.J. Miller, S.J. Zhang, H.P. Li, Y.F. Ho, K.A. Schwehr, D.I. Kaplan, S. Otosaka, K.A. Roberts, R. Brinkmeyer, C.M. Yeager, P.H. Santschi, Sequestration and remobilization of radioiodine (I-129) by soil organic matter and possible consequences of the remedial action at Savannah River site, *Environ. Sci. Technol.* 45 (2011) 9975–9983.
- [14] W.H. Shetaya, S.D. Young, M.J. Watts, E.L. Ander, E.H. Bailey, Iodine dynamics in soils, *Geochim. Cosmochim. Acta* 77 (2012) 457–473.
- [15] S. Choung, M. Kim, J.S. Yang, M.G. Kim, W. Um, Effects of radiation and temperature on iodide sorption by surfactant-modified bentonite, *Environ. Sci. Technol.* 48 (2014) 9684–9691.
- [16] H. Inoue, M. Kagoshima, M. Yamasaki, Y. Honda, Radioactive iodine waste treatment using electro dialysis with an anion exchange paper membrane, *Appl. Radiat. Isot.* 61 (2004) 1189–1193.
- [17] K. Morimoto, K. Tamura, Y. Umemura, H. Sato, A. Yamagishi, Capture of radioactive nuclear wastes from sea water by use of clay minerals, *Chem. Lett.* 40 (2011) 867–869.
- [18] R.F. de Luis, A. Martinez-Amesti, E.S. Larrea, L. Lezama, A.T. Aguayo, M.I. Arriortua, Composite beta- $\text{AgVO}_3@V_5^{+}V_6^{4+}O_{4.8}$ hydrogels and xerogels for iodide capture, *J. Mater. Chem. A* 3 (2015) 19996–20012.
- [19] D.J. Yang, H.W. Liu, L. Liu, S. Sarina, Z.F. Zheng, H.Y. Zhu, Silver oxide nanocrystals anchored on titanate nanotubes and nanofibers: promising candidates for entrapment of radioactive iodine anions, *Nanoscale* 5 (2013) 11011–11018.
- [20] A. Bo, S. Sarina, Z.F. Zheng, D.J. Yang, H.W. Liu, H.Y. Zhu, Removal of radioactive iodine from water using Ag_2O grafted titanate nanolamina as efficient adsorbent, *J. Hazard. Mater.* 246 (2013) 199–205.
- [21] S. Sarina, A. Bo, D. Liu, H. Liu, D. Yang, C. Zhou, N. Maes, S. Komarneni, H. Zhu, Separate or simultaneous removal of radioactive cations and anions from water by layered sodium vanadate-based sorbents, *Chem. Mater.* 26 (2014) 4788–4795.
- [22] D.J. Yang, S. Sarina, H.Y. Zhu, H.W. Liu, Z.F. Zheng, M.X. Xie, S.V. Smith, S. Komarneni, Capture of radioactive cesium and iodide ions from water by using titanate nanofibers and nanotubes, *Angew. Chem., Int. Ed.* 50 (2011) 10594–10598.
- [23] S.S. Liu, N. Wang, Y.C. Zhang, Y.R. Li, Z. Han, P. Na, Efficient removal of radioactive iodide ions from water by three-dimensional $\text{Ag}_2\text{O}-\text{Ag}/\text{TiO}_2$ composites under visible light irradiation, *J. Hazard. Mater.* 284 (2015) 171–181.
- [24] W.J. Mu, X.L. Li, G.P. Liu, Q.H. Yu, X. Xie, H.Y. Wei, Y. Jian, Safe disposal of radioactive iodide ions from solutions by Ag_2O grafted sodium niobate nanofibers, *Dalton Trans.* 45 (2016) 753–759.
- [25] A. Bo, S. Sarina, H. Liu, Z. Zheng, Q. Xiao, Y. Gu, G.A. Ayoko, H. Zhu, Efficient removal of cationic and anionic radioactive pollutants from water using hydroxalite-based getters, *ACS Appl. Mater. Interfaces* 8 (2016) 16503–16510.
- [26] C. Chen, O.G. Apul, T. Karanfil, Removal of bromide from surface waters using silver impregnated activated carbon, *Water. Res.* 113 (2017) 223–230.
- [27] K.W. Chapman, P.J. Chupas, T.M. Nenoff, Radioactive iodine capture in silver-containing mordenites through nanoscale silver iodide formation, *J. Am. Chem. Soc.* 132 (2010) 8897–8899.
- [28] F.L. Theiss, S.J. Couperthwaite, G.A. Ayoko, R.L. Frost, A review of the removal of anions and oxyanions of the halogen elements from aqueous solution by layered double hydroxides, *J. Colloid Interface Sci.* 417 (2014) 356–368.
- [29] F.L. Theiss, G.A. Ayoko, R.L. Frost, Leaching of iodide (I^-) and iodate (IO_3^-) anions from synthetic layered double hydroxide materials, *J. Colloid Interface Sci.* 478 (2016) 311–315.
- [30] F.L. Theiss, G.A. Ayoko, R.L. Frost, Iodide removal using LDH technology, *Chem. Eng. J.* 296 (2016) 300–309.
- [31] F.L. Theiss, G.A. Ayoko, R.L. Frost, Sorption of iodide (I^-) from aqueous solution using Mg/Al layered double hydroxides, *Mater. Sci. Eng. C* 77 (2017) 1228–1234.

- [32] S.D. Balsley, P.V. Brady, J.L. Krumhansl, H.L. Anderson, Iodide retention by metal sulfide surfaces: Cinnabar and chalcocite, *Environ. Sci. Technol.* 30 (1996) 3025–3027.
- [33] S.W. Liu, S.H. Kang, H.M. Wang, G.Z. Wang, H.J. Zhao, W.P. Cai, Nanosheets-built flowerlike micro/nanostructured $\text{Bi}_2\text{O}_{2.33}$ and its highly efficient iodine removal performances, *Chem. Eng. J.* 289 (2016) 219–230.
- [34] Y. Liu, P. Gu, L. Jia, G.H. Zhang, An investigation into the use of cuprous chloride for the removal of radioactive iodide from aqueous solutions, *J. Hazard. Mater.* 302 (2016) 82–89.
- [35] P. Mao, L.Y. Qi, X.D. Liu, Y. Liu, Y. Jiao, S.W. Chen, Y. Yang, Synthesis of $\text{Cu}/\text{Cu}_2\text{O}$ hydrides for enhanced removal of iodide from water, *J. Hazard. Mater.* 328 (2017) 21–28.
- [36] K. Watson, M.J. Farre, N. Knight, Strategies for the removal of halides from drinking water sources, and their applicability in disinfection by-product minimisation: a critical review, *J. Environ. Manage.* 110 (2012) 276–298.
- [37] C. Li, Z. Zhuang, F. Huang, Z. Wu, Y. Hong, Z. Lin, Recycling rare earth elements from industrial wastewater with flowerlike nano- $\text{Mg}(\text{OH})_2$, *ACS Appl. Mater. Interfaces* 5 (2013) 9719–9725.
- [38] B.J. Li, H.Q. Cao, G. Yin, $\text{Mg}(\text{OH})_2$ @reduced graphene oxide composite for removal of dyes from water, *J. Mater. Chem.* 21 (2011) 13765–13768.
- [39] W.Z. Liu, F. Huang, Y.J. Wang, T. Zou, J.S. Zheng, Z. Lin, Recycling $\text{Mg}(\text{OH})_2$ nanoadsorbent during treating the low concentration of Cr^{VI} , *Environ. Sci. Technol.* 45 (2011) 1955–1961.
- [40] Y.J. Wang, J.P. Chen, L.L. Lu, Z. Lin, Reversible switch between bulk MgCO_3 center dot $3\text{H}_2\text{O}$ and $\text{Mg}(\text{OH})_2$ micro/nanorods induces continuous selective preconcentration of anionic dyes, *ACS Appl. Mater. Interfaces* 5 (2013) 7698–7703.
- [41] B.B. Jia, J.N. Wang, J. Wu, C.J. Li, “Flower-Like” $\text{PA6}/\text{Mg}(\text{OH})_2$ electrospun nanofibers with $\text{Cr}(\text{VI})$ -removal capacity, *Chem. Eng. J.* 254 (2014) 98–105.
- [42] Z.P. Wang, C.H. Li, Y. Mu, Z. Lin, A.J. Yi, Q. Zhang, B. Yan, Nanoadduct relieves: alleviation of developmental toxicity of $\text{Cr}(\text{VI})$ due to its spontaneous adsorption to $\text{Mg}(\text{OH})_2$ nanoflakes, *J. Hazard. Mater.* 287 (2015) 296–305.
- [43] M.H. Liu, Y.H. Wang, L.T. Chen, Y. Zhang, Z. Lin, $\text{Mg}(\text{OH})_2$ supported nanoscale zero valent iron enhancing the removal of $\text{Pb}(\text{II})$ from aqueous solution, *ACS Appl. Mater. Interfaces* 7 (2015) 7961–7969.
- [44] C. Liang, T. Sasaki, Y. Shimizu, N. Koshizaki, Pulsed-laser ablation of Mg in liquids: surfactant-directing nanoparticle assembly for magnesium hydroxide nanostructures, *Chem. Phys. Lett.* 389 (2004) 58–63.
- [45] P.P. Wang, Y.X. Ye, D.W. Liang, H.M. Sun, J. Liu, Z.F. Tian, C.H. Liang, Layered mesoporous $\text{Mg}(\text{OH})_2/\text{GO}$ nanosheet composite for efficient removal of water contaminants, *RSC Adv.* 6 (2016) 26977–26983.
- [46] Z. Chen, Z.Y. Zhuang, Q. Cao, X.H. Pan, X. Guan, Z. Lin, Adsorption-induced crystallization of U-Rich nanocrystals on nano- $\text{Mg}(\text{OH})_2$ and the aqueous uranyl enrichment, *ACS Appl. Mater. Interfaces* 6 (2014) 1301–1305.
- [47] D.K. Aswal, K.P. Muthe, S. Tawde, S. Chodhury, N. Bagkar, A. Singh, S.K. Gupta, J. V. Yakhmi, XPS and AFM investigations of annealing induced surface modifications of MgO single crystals, *J. Cryst. Growth.* 236 (2002) 661–666.
- [48] L.X. Li, D. Xu, X.Q. Li, W.C. Liu, Y. Jia, Excellent fluoride removal properties of porous hollow MgO microspheres, *New. J. Chem.* 38 (2014) 5445–5452.
- [49] H.Q. Wang, J.Z. Li, M.J. Zhou, Q.F. Guan, Z.Y. Lu, P.W. Huo, Y.S. Yan, Preparation and characterization of $\text{Ag}_2\text{O}/\text{SWNTs}$ photocatalysts and its photodegradation on tetracycline, *J. Ind. Eng. Chem.* 30 (2015) 64–70.
- [50] L. Shi, L. Liang, J. Ma, F.X. Wang, J.M. Sun, Enhanced photocatalytic activity over the $\text{Ag}_2\text{O}-g\text{-C}_3\text{N}_4$ composite under visible light, *Catal. Sci. Technol.* 4 (2014) 758–765.
- [51] M. Xu, L. Han, S.J. Dong, Facile fabrication of highly efficient $g\text{-C}_3\text{N}_4/\text{Ag}_2\text{O}$ heterostructured photocatalysts with enhanced visible-light photocatalytic activity, *ACS Appl. Mater. Interfaces* 5 (2013) 12533–12540.
- [52] G. Leofanti, M. Padovan, G. Tozzola, B. Venturini, Surface area and pore texture of catalysts, *Catal. Today* 41 (1998) 207–219.
- [53] V. Srivastava, Y.C. Sharma, M. Sillanpaa, Green synthesis of magnesium oxide nanoflower and its application for the removal of divalent metallic species from synthetic wastewater, *Ceram. Int.* 41 (2015) 6702–6709.
- [54] C.M. Xiong, W. Wang, F.T. Tan, F. Luo, J.G. Chen, X.L. Qiao, Investigation on the efficiency and mechanism of $\text{Cd}(\text{II})$ and $\text{Pb}(\text{II})$ removal from aqueous solutions using MgO nanoparticles, *J. Hazard. Mater.* 299 (2015) 664–674.
- [55] G. Jordan, W. Rammensee, Dissolution rates and activation energy for dissolution of brucite (001): a new method based on the microtopography of crystal surfaces, *Geochim. Cosmochim. Acta* 60 (1996) 5055–5062.
- [56] Q. Cao, F. Huang, Z.Y. Zhuang, Z. Lin, A study of the potential application of nano- $\text{Mg}(\text{OH})_2$ in adsorbing low concentrations of uranyl tricarbonate from water, *Nanoscale* 4 (2012) 2423–2430.
- [57] H.C. Pang, G.L. Ning, W.T. Gong, J.W. Ye, Y. Lin, Direct synthesis of hexagonal $\text{Mg}(\text{OH})_2$ nanoplates from natural brucite without dissolution procedure, *Chem. Commun.* 47 (2011) 6317–6319.
- [58] R. Li, P. Li, J. Cai, S.J. Xiao, H. Yang, A.M. Li, Efficient adsorption of both methyl orange and chromium from their aqueous mixtures using a quaternary ammonium salt modified chitosan magnetic composite adsorbent, *Chemosphere* 154 (2016) 310–318.
- [59] O.S. Pokrovsky, J. Schott, Experimental study of brucite dissolution and precipitation in aqueous solutions: surface speciation and chemical affinity control, *Geochim. Cosmochim. Acta* 68 (2004) 31–45.
- [60] J.M. Hanlon, L.B. Diaz, G. Balducci, B.A. Stobbs, M. Bielewski, P. Chung, I. MacLaren, D.H. Gregory, Rapid surfactant-free synthesis of $\text{Mg}(\text{OH})_2$ nanoplates and pseudomorphic dehydration to MgO , *Cryst. Eng. Comm.* 17 (2015) 5672–5679.
- [61] A. Godon, N. Jendrzewski, H.G.M. Eggenkamp, D.A. Banks, M. Ader, M.L. Coleman, F. Pineau, A cross-calibration of chlorine isotopic measurements and suitability of seawater as the international reference material, *Chem. Geol.* 207 (2004) 1–12.
- [62] J. Zhao, K. Yu, Y.N. Hu, S.J. Li, X. Tan, F.W. Chen, Z.M. Yu, Discharge behavior of $\text{Mg}-4\text{ wt}\%\text{Ga}-2\text{ wt}\%\text{Hg}$ alloy as anode for seawater activated battery, *Electrochim. Acta* 56 (2011) 8224–8231.
- [63] L. Newsome, K. Morris, J.R. Lloyd, The biogeochemistry and bioremediation of uranium and other priority radionuclides, *Chem. Geol.* 363 (2014) 164–184.
- [64] Q.L. Fang, S.X. Duan, J.F. Zhang, J.X. Li, K.C.F. Leung, Dual shelled $\text{Fe}_3\text{O}_4/\text{polydopamine}$ hollow microspheres as an effective $\text{Eu}(\text{III})$ adsorbent, *J. Mater. Chem. A* 5 (2017) 2947–2958.
- [65] X.L. Han, M.Y. Xu, S. Yang, J. Qian, D.B. Hua, Acetylcysteine-functionalized microporous conjugated polymers for potential separation of uranium from radioactive effluents, *J. Mater. Chem. A* 5 (2017) 5123–5128.
- [66] Z.Y. Zhuang, H. Chen, Z. Lin, Z. Dang, Mn_2O_3 hollow spheres synthesized based on an ion-exchange strategy from amorphous calcium carbonate for highly efficient trace-level uranyl extraction, *Environ. Sci. Nano* 3 (2016) 1254–1258.